

La_{0.6}Sr_{0.4}Cr_{0.8}Co_{0.2}O₃ Perovskite Decorated with Exsolved Co Nanoparticles for Stable CO₂ Splitting and Syngas Production

Alfonso J. Carrillo, Kun Joong Kim, Zachary D. Hood, Alexander H. Bork, and Jennifer L. M. Rupp*

Cite This: <https://dx.doi.org/10.1021/acsaem.0c00249>

Read Online

ACCESS |



Metrics & More



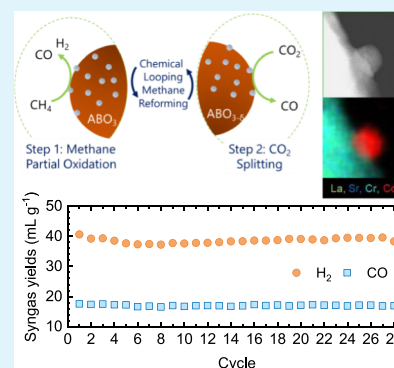
Article Recommendations



Supporting Information

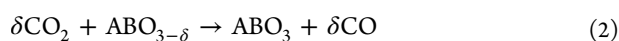
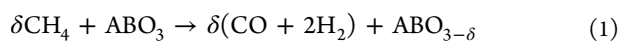
ABSTRACT: Exsolution is an auspicious processing route for the fabrication of catalytically active nanoparticles that are anchored into the oxide backbone, presenting inherent long-term stability benefits. Here, we show that the exsolution method can be effectively applied to create metallic nanoparticles that improve the syngas production performance under chemical-looping methane reforming coupled with CO₂ splitting. The La_{0.6}Sr_{0.4}Cr_{0.8}Co_{0.2}O₃ perovskite surface was functionalized with exsolving metallic Co nanoparticles of around 30 nm which exhibited remarkable microstructural stability and uniform dispersion after 28 cycles at 900 °C. The highly dispersed exsolved nanoparticles activated methane partial oxidation, increasing the syngas selectivity and fuel production rates, namely, 44 mL_{H₂} min⁻¹ g⁻¹, which was a twofold improvement over the bare perovskite. In addition, surface modification *via* exsolution enhanced the CO₂-splitting rate, *ca.* 100 mL_{CO} min⁻¹ g⁻¹, faster than that of state-of-the-art ceria, *ca.* 70 mL_{CO} min⁻¹ g⁻¹. The results illustrate that exsolved nanoparticles play a critical role in improving the fuel production performance while presenting high durability, denoting its relevance for high-temperature thermocatalytic processes for syngas production.

KEYWORDS: exsolution, Co nanoparticles, perovskites, chemical looping, methane reforming, CO₂ splitting



1. INTRODUCTION

Chemical looping reforming coupled with CO₂ splitting has emerged as a promising route for the production of sustainable fuels because of its versatility in terms of gas separation and process intensification.¹ This technology consists of two main steps: in the first step, methane reacts with the lattice oxygen of a metal oxide, in this case, a perovskite, ABO₃, producing hydrogen and carbon monoxide (syngas) in a 2:1 molar ratio, eq 1, which is ideal for further processing of syngas into liquid fuels through the Fischer–Tropsch process.² Importantly, this endothermic reaction occurring at temperatures from 700 to 1000 °C, known as methane partial oxidation (MPO), could be driven utilizing concentrated solar power^{3,4} or industrial waste heat.⁵ In the second step, CO₂ reacts with the reduced perovskite, ABO_{3-δ}, replenishing the lattice oxygen with the subsequent formation of CO (eq 2). This step could also be performed by the simultaneous splitting of CO₂ and H₂O, producing syngas.



Here, δ denotes the oxygen nonstoichiometry, namely, the perovskite's extent of reduction, which directly correlates with the amount of fuel produced in each step. Thus, it is crucial to choose materials with high oxygen exchange capacity and stability, in order to guarantee the feasibility of this process.³

Binary oxides such as ferrites⁶ or spinels⁷ normally present a high oxygen exchange capacity; however, these materials exhibit slow kinetics and structural instability^{3,7,8} or low selectivity toward CO.⁹ In this respect, Gao *et al.* recently discovered that Ce-doped Mn oxides exhibited a quite stable chemical looping reforming performance, in which the intermediate formation of Mn carbide favored the oxygen exchange capacity and syngas production.^{10,11} On the other hand, nonstoichiometric redox oxides present higher chemical stability. Among them, ceria has been extensively studied^{2,3,5,12–18} and even tested in solar-driven reactors.^{19,20} In this respect, Warren *et al.* recently reported a solar-driven indirectly irradiated packed bed with a solar-to-fuel efficiency of 10.06% using ceria as a redox intermediate,²¹ which is a twofold increase if compared with the highest solar-to-fuel efficiency obtained in conventional solar-driven CO₂ splitting, 5.25% by Marxer *et al.*²²

However, ceria presents limited oxygen exchange capacity. In this respect, perovskite oxides^{23–29} have attracted considerable attention because of their easy compositional

Received: February 5, 2020

Accepted: April 10, 2020

Published: April 10, 2020



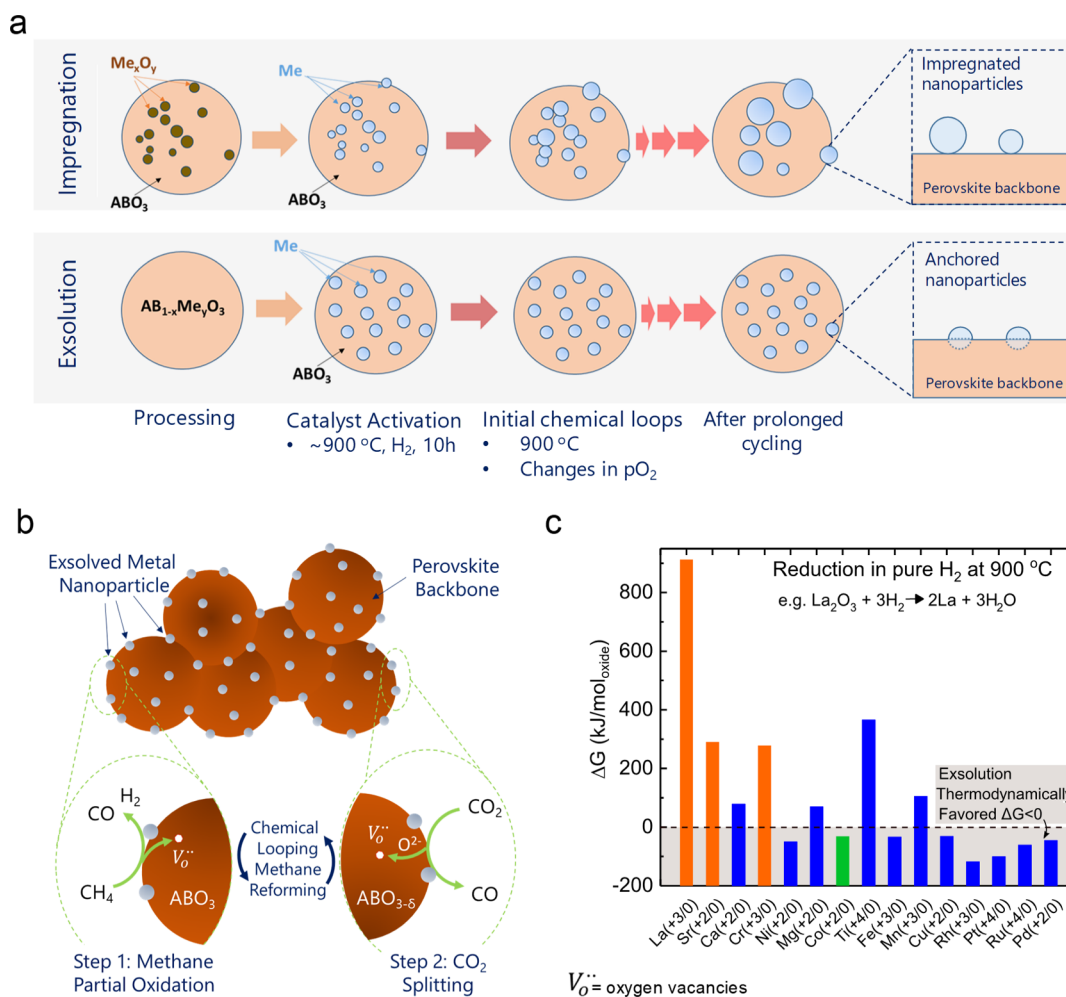
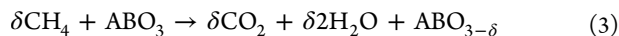


Figure 1. (a) Schematic comparing the main differences that exsolution or impregnation cermet manufacturing poses on the catalytic nanoparticle stability in a chemical looping operation. (b) Schematic depicting the chemical looping reforming of methane coupled with CO₂-splitting, using exsolution-promoted perovskites. (c) Gibbs free energy for the reduction of representative cations present in perovskites (ABO₃) into their metallic form. According to this plot, A-site cations, La, Sr, and Cr on the B-site do not exsolve as metallic particles, whereas, Co is thermodynamically favored to exsolve as the metal on the perovskite surface. Thermodynamic calculations were performed with HSC Chemistry Oy 6.1.

and structural tunability³⁰ that can be used to design materials with higher oxygen exchange capacity (δ) than ceria⁷ and high chemical stability.

Additionally, it is critical that no parasitic reactions take place, which affect the overall fuel production. Namely, during the reduction step, CH₄ can combust to produce CO₂ and H₂O, eq 3, which limits the selectivity toward syngas. CH₄ could also decompose into solid carbon and H₂, eq 4, which produces deviations from the ideal H₂/CO molar ratio of 2:1, and coking, which can be detrimental for the chemical activity of the catalyst. In the case of performing the oxidation under a CO₂ atmosphere, the deposited carbon can transform into CO by the *Boudouard* reaction, eq 5, regenerating the catalyst.



In order to avoid secondary reactions, incorporation of metallic promoters, such as Rh or Ni, onto the oxygen carrier has been employed to enhance the surface activity of oxide and favor methane activation.^{27,29,31,32} Such metallic nanoparticles

are normally prepared *via* impregnation routes.³³ However, the elevated temperatures (*e.g.*, 700–1000 °C) at which chemical looping reforming takes place can lead to nanoparticle agglomeration³⁴ or Ostwald ripening,³⁵ which alters the nanoparticle microstructure, decreasing the chemical performance over prolonged cycling.

In this respect, the exsolution method emerges as a promising alternative to achieve highly dispersed and stable metallic nanoparticles.³⁶ Generally, in the exsolution process, cations contained in the oxide crystal structure migrate to the oxide surface under reductive atmospheres, leading to the creation of metallic nanoparticles.³⁷ Importantly, such exsolved nanoparticles remain anchored to the perovskite backbone, avoiding agglomeration at high temperatures as compared to nanoparticles prepared by impregnation, Figure 1a. It is important to note that metallic nanoparticle exsolution of precious metals such as Ru,³⁸ Pd,³⁹ Rh, or Pt⁴⁰ or transition metals such as Co,⁴¹ Fe,⁴¹ Ni,^{36,42–44} or alloys thereof^{45–48} has been widely investigated in the field of solid oxide fuel cells (SOFCs).⁴⁹ Many benefits arise from the high surface affinity between the anchored metallic nanoparticle and the perovskite backbone, such as resistance against carbon deposition and particle coarsening⁵⁰ or better long-term performance under

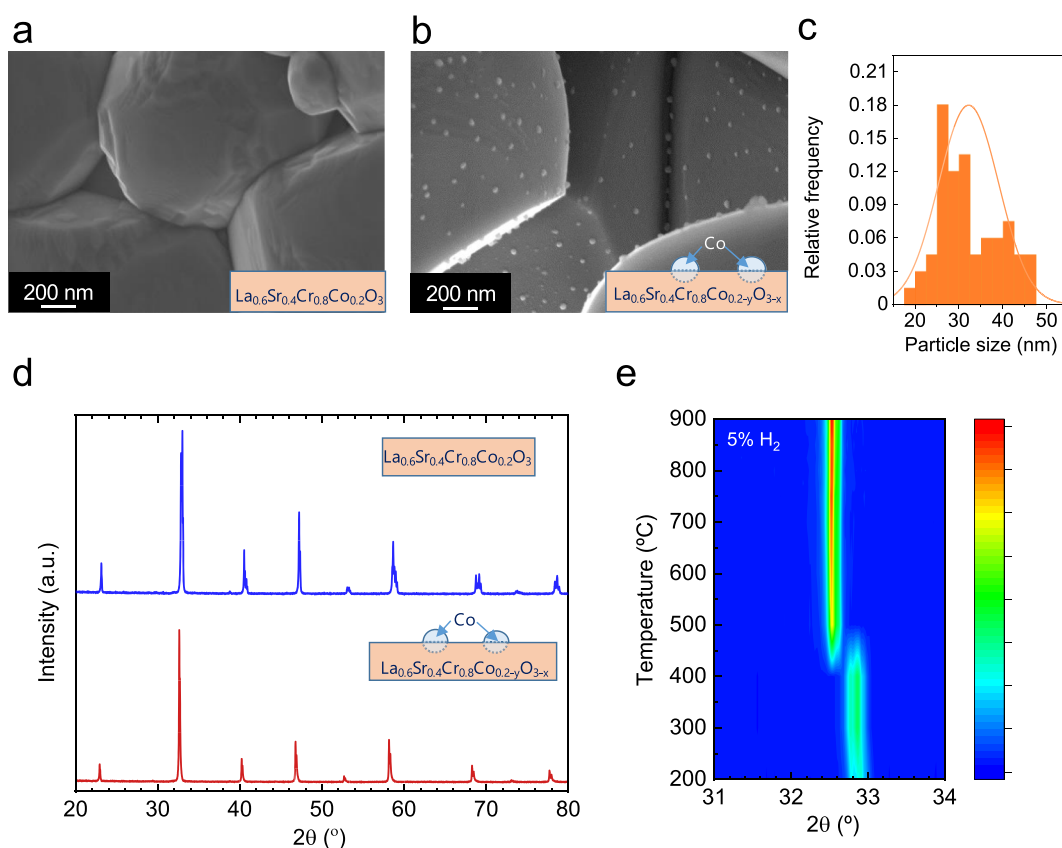


Figure 2. SEM images comparing LSCC (a) before and (b) after exsolution at 900 °C in an atmosphere of 5% H₂ for 10 h. (c) Particle size distribution histogram of the exsolved nanoparticles on LSCC. (d) XRD patterns of the perovskite before and after exsolution. (e) *In situ* XRD analysis performed to LSCC, heating up to 900 °C under 5% H₂/Ar. The color bar on the right panel indicates the peak intensity (red, most intense).

CO oxidation catalytic tests compared to commercial noble metal-supported catalysts.⁴⁷ Thus, very recently, it has also motivated its application in chemical looping reforming of methane. Hosseini *et al.* observed the *in situ* formation of exsolved nanoparticles (Cu and Fe–Ni alloy) that enhanced the hydrogen yields in chemical looping reforming coupled with H₂O splitting.⁵¹ Otto *et al.* assessed Ni exsolution on La_{0.5}Ca_{0.4}Ti_{0.8}Ni_{0.2}O_{3-δ} for chemical looping reforming, exhibiting improved performance when compared with the bare perovskite without nanoparticle exsolution, and importantly, with respect to a material with the same composition but in which the Ni nanoparticles were added *via* impregnation.⁵² Interestingly, the same group recently demonstrated that during the exsolution process, nanoparticles could grow submerged in the oxide bulk, which enhanced the oxygen exchange.⁵³ In both studies, the re-oxidation reaction was carried out under air, leading to the transformation of exsolved Ni nanoparticles into NiO. Till date, chemical looping reforming coupled with CO₂ splitting has not been explored for exsolution-promoted perovskites, which is an interesting process from an industrial point of view, for example, for the production of acetic acid *via* the Cativa process.⁵ To the best of our knowledge, the application of exsolution-functionalized perovskites on methane reforming coupled with CO₂ splitting has only been tested by Dimitrakopoulos *et al.* using a perovskite-based membrane reactor, in which exsolved nanoparticles were generated *in situ* during the reaction.⁵⁴

Thus, in this work, we design and fabricate perovskite-based redox catalysts *via* nanoparticle exsolution for chemical looping

methane reforming coupled with CO₂ splitting, Figure 1b. We have chosen La_{0.6}Sr_{0.4}Cr_{0.8}Co_{0.2}O₃ (LSCC) as the oxygen carrier because of its favorable thermodynamics for CO₂ splitting and high-temperature thermochemical stability.⁵⁵ Furthermore, thermodynamic calculations indicate that metallic cobalt will be the only exsolved species, Figure 1c, which is a well-known methane reforming catalyst.⁵⁶ This matches well with previous studies that report Co exsolution on La_{0.7}Sr_{0.3}Cr_{0.85}Co_{0.15}O₃ SOFC anodes.⁵⁷ Thus, we hypothesize that exsolved Co nanoparticles anchored in the LSCC backbone will catalyze the reforming reaction, while exhibiting high microstructural stability under prolonged cycling, matching suitably with the CO₂-splitting ability of the selected perovskite.

2. RESULTS AND DISCUSSION

2.1. Understanding Co Exsolution on LSCC. LSCC perovskite powder was prepared using the Pechini method (see the **Experimental Procedures** for details). Exsolved cobalt nanoparticles were created by exposing the LSCC sample to a reducing atmosphere of 5% H₂/Ar at 900 °C for 10 h to form exsolution-decorated LSCC (exLSCC). Under these conditions, reduction of Co cations into metallic Co is thermodynamically favorable, see Figure 1c, which indicates that this system will preferentially exsolve metallic Co nanoparticles to the surface and not Cr, La, or Sr. A comparison of the morphology of the perovskite before and after the exsolution treatment is depicted in Figure 2. Before the exsolution treatment, Figure 2a, LSCC presents a

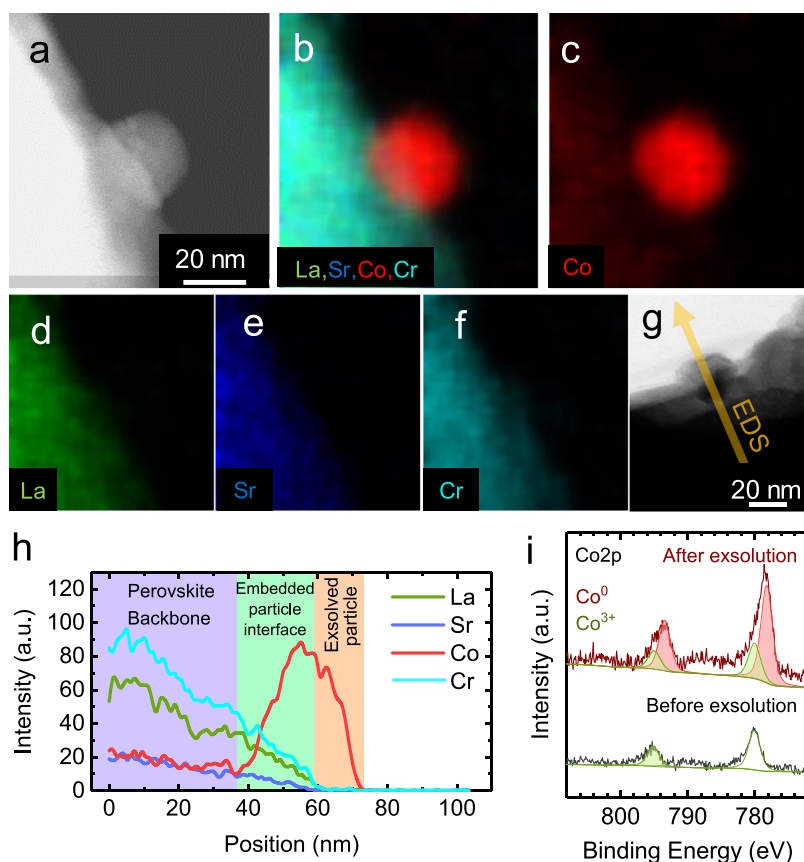


Figure 3. (a) HAADF-STEM image and (b–f) EDS elemental mappings of LSCC after exsolution (exLSCC). (g,h) Bright field-STEM image and EDS line scan of the perovskite outer layers and an exsolved nanoparticle in exLSCC. (i) XPS spectra comparing the Co 2p signal of LSCC perovskite before and after exsolution. Before XPS analyses, the perovskite after exsolution was stored in an oxygen-free atmosphere in order to avoid the formation of Co_3O_4 .

microstructure formed by micron-sized particles with rounded edges. After exposure to H_2 , the perovskite powder surface significantly changed with the appearance of well-dispersed nanoparticles over the micron-sized perovskite grains, which is an indication of successful nanoparticle exsolution, Figure 2b. Nanoparticles were grown on the particle surface and at the rounded edges of the perovskite grains, exhibiting a bimodal nanoparticle distribution, with an average particle size of 32 ± 7 nm, Figure 2c.

X-ray diffraction (XRD) was used to analyze the perovskite crystal phase before and after exsolution, Figure 2d. It was observed that the perovskite samples crystallized in the rhombohedral phase, which prevailed after exsolution, correlated well with a previous report.⁵⁵ Cell volumes were determined by Rietveld refinement (see Figure S1 in the Supporting Information), indicating lattice expansion upon exsolution. Namely, the cell volumes were 351.37 and 342.74 \AA^3 for exLSCC and LSCC, respectively. The exsolution treatment of LSCC was studied *via in situ* XRD under reducing conditions (5 vol % H_2 in Ar) while heating up to 900 $^\circ\text{C}$, Figure 2e, revealing that there is a peak shift of *ca.* 0.25 $^\circ$ toward lower 2θ values taking place between 400 and 500 $^\circ\text{C}$. This change is ascribed to lattice expansion induced by oxygen release, which matches well with data found in the literature for similar perovskite compositions.^{43,58} Namely, thermogravimetric analysis by Papargyriou *et al.* revealed that the oxygen loss of Cr-based perovskite oxide took place in the 400–500 $^\circ\text{C}$ range when heated up under a 5% H_2/Ar atmosphere.⁶⁰

Although the presence of exsolved nanoparticles was inferred by scanning electron microscopy (SEM), metallic Co reflections were not observed in XRD studies because of the phase ratio of metallic Co being below the detection limit, as previously pointed out for exsolved nanoparticles.⁵⁸ In future studies, more powerful tools such as neutron powder diffraction or high resolution XRD⁵³ will be used to scrutinize the presence of metallic Co in the diffraction patterns.

Thus, to determine the chemistry and habitus of the exsolved nanoparticles on the LSCC perovskite, we turn to electron microscopy, Figure 3. A high-angle annular dark-field scanning transmission electron microscopy (HAADF-STEM) image of an exsolved nanoparticle with a size of *ca.* 35 nm on the surface of the LSCC is displayed in Figure 3a. We used energy-dispersive X-ray spectroscopy (EDS) mapping to confirm the elemental distribution of La, Sr, Cr, and Co on the exsolved nanoparticle and the perovskite backbone of the cermet structure, Figure 3b–f. EDS elemental mapping clearly shows that the exsolved nanoparticles are composed just of Co, while the perovskite backbone is composed of La, Sr, Cr, and Co. Through an EDS line scan of the perovskite backbone and into the exsolved Co nanoparticle, we find that the relative concentration of La and Cr was higher than that of Sr and Co, which is expected based on the perovskite stoichiometry, Figure 3g. It was observed that the relative amount of Co is higher than expected, showing similar values as Sr. Namely, both elements presented a relative intensity of *ca.* 20 a.u. at the start of the scan, which might indicate Co enrichment and/or

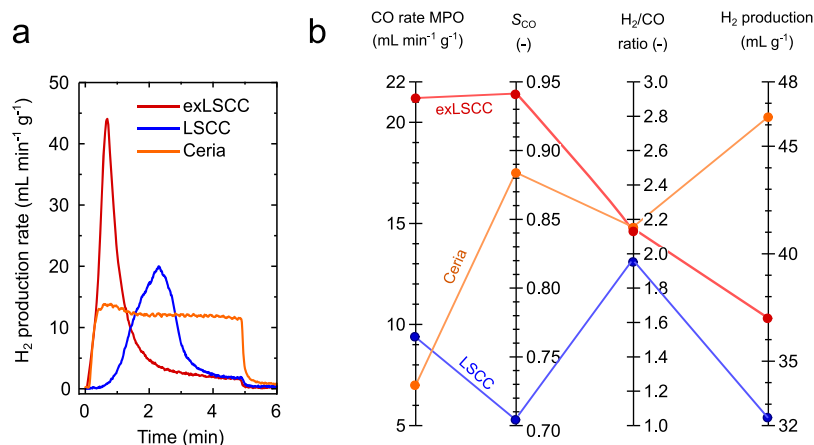


Figure 4. (a) H₂ production rate comparison for the MPO half cycle carried out at 900 °C and 5 min of 5 vol % CH₄ injections (15 mL min⁻¹ CH₄ balanced with Ar, total flow 300 mL min⁻¹). (b) Comparison of the key metrics for the MPO (CO rate, selectivity to CO, S_{CO}, total H₂ production, and H₂ to CO ratio).

Sr depletion close to the surface upon exsolution. As shown both in the line scan and the EDS elemental mappings, an interfacial zone of 20 nm exists where a sharp increase in the Co concentration and a gradual decrease in the La, Sr, and Cr contributions occur. The interface between the perovskite and the exsolved nanoparticles is still rich in all four elements, suggesting that these nanoparticles are intimately anchored to the surface of the perovskite. The nanoparticle anchoring poses obvious advantages in the catalysis when compared with other methods such as infiltration, especially from the stability point of view, because agglomeration or coarsening with neighboring particles is avoided. Additionally, anchoring is beneficial in reducing the formation of carbon depositions, as demonstrated by Neagu *et al.*⁵⁰

X-ray photoelectron spectroscopy (XPS) was employed to further understand the surface chemistry of LSCC before and after exsolution, Figure 3h. XPS analyses of La, Sr, Cr, and O before and right after exsolution are shown in Figure S2d in the Supporting Information. In the case of La 3d spectra, there were no major changes before and after exsolution as illustrated by the differences in the La 3d_{5/2} peak binding energies ΔE of ~ 4.1 and ~ 3.9 eV before and after exsolution, respectively. Regarding the Sr 3d spectra, the main differences arising from the exsolution process were related to the decrease of the Sr²⁺ peak intensity (BE ≈ 230 eV) after exsolution, which correlates well with the Sr depletion observed in the EDS analyses, as shown in Figure 3h, on the surface of the exsolved perovskite. XPS analyses of the O 1s peaks indicated, as expected, that exsolution resulted in the creation of oxygen vacancies. In the spectra for the as-synthesized material, LSCC, the intensity of the lattice O peak (~ 528.8 eV) is higher than that for the peak related to oxygen vacancies (~ 531.2 eV), where the opposite is true for the exsolved material (exLSCC). These results confirmed the lattice expansion induced by the creation of oxygen vacancies during the exsolution process. Part of the H₂ that is used for the exsolution treatment reacts with the perovskite lattice oxygen with concomitant production of oxygen vacancies and H₂O. On the B-site, XPS revealed the most probable presence of SrCrO₄ surface segregations before exsolution, denoted by the appearance of a peak around 580 eV in the Cr 2p spectra, commonly observed in Sr-doped chromates, which disappears upon reduction.⁵⁹ Before exsolution, the surface Co was in the +3 oxidation state,

exhibited as a peak around 780 eV. Directly after exsolution, the Co 2p spectrum revealed the presence of Co⁰ peak at 778 eV, consistent with high-resolution (HR)-TEM analysis. This result confirms that Co cations located in the perovskite lattice can be selectively reduced to metallic Co and diffuse out on the surface. Still, exposure of metallic Co to an oxygen-rich atmosphere is expected to oxidize the metallic Co to Co₃O₄, forming core-shell nanoparticles on the surface of LSCC. Importantly, the oxidation of metallic Co with CO₂ or H₂O is not thermodynamically favored. Therefore, it is not expected that exsolved metallic Co nanoparticles will become passivated during the CO₂-splitting half cycle.

In this section, we have determined the nature of the exsolved nanoparticle cobalt species. It should be noted that under the reducing/oxidizing experimental conditions of the chemical looping MPO test, for example, CH₄ and CO₂ pulses, it is expected that metallic Co will be the active catalytic phase of the exsolved metal particles on the perovskite backbone, as revealed by XPS and TEM analyses.

2.2. Chemical Looping MPO. Chemical looping reforming tests were performed in a high-temperature fixed-bed reactor. The performance of the exsolution-promoted perovskite, exLSCC, is benchmarked against CeO₂, one of the reference materials³ in thermochemical syngas production, and the perovskite without nanoparticle decoration, LSCC. Figure 4a depicts the H₂ production rate of the first half cycle, in which CH₄ (5 vol %, balanced with Ar) was injected for 5 min. The exsolution-treated perovskite, exLSCC, exhibited the fastest syngas production rates among the three materials tested in this work. Namely, its H₂ production peak rate was 43.9 mL min⁻¹ g⁻¹, whereas LSCC and ceria showed 19.7 and 13.0 mL min⁻¹ g⁻¹, respectively. As expected from the literature,² ceria exhibits slow and steady MPO reaction rates. On the other hand, exLSCC shows a sharp peak that reaches the maximum H₂ production in 0.5 min after CH₄ injection. These results indicate that the MPO could be performed in shorter methane pulses when utilizing exLSCC as a reacting media because most of the syngas production occurs in about 2 min, which will have a positive effect on the efficiency of the process. To put these results into perspective, Fe₂O₃@La_{0.8}Sr_{0.2}FeO_{3- δ} core-shell materials exhibited a maximum H₂ peak after *ca.* 7 min.²⁴ Regarding the non-exsolution-treated perovskite, LSCC, the peak rate occurs after

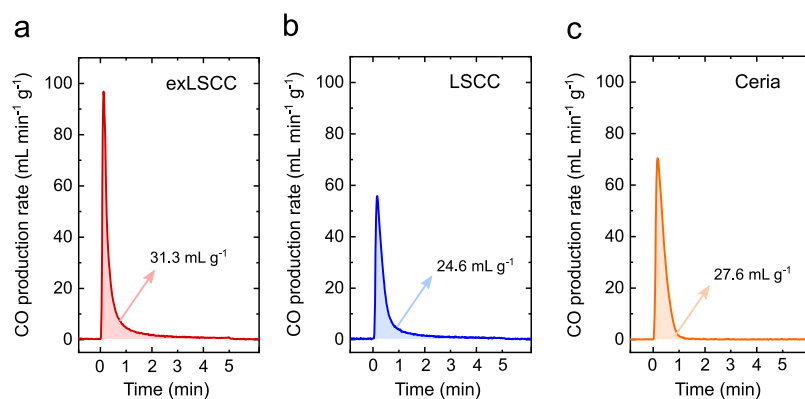


Figure 5. CO₂-splitting rate curves for (a) exsolution-promoted LSCC (exLSCC), (b) LSCC, and (c) CeO₂. Reactions were performed at 900 °C, with 5 min CO₂ injections (16 vol %). Prior to the CO₂-splitting reaction, materials were reduced under a 5 vol % CH₄ gas stream (300 mL min⁻¹ total flow) at 900 °C, for 5 min.

2.2 min, denoting a slower H₂ production. The fact that the exsolution-promoted sample, exLSCC, displays a twofold faster fuel production rate compared to the bare perovskite LSCC could indicate that exsolved Co nanoparticles act as reaction sites for methane activation, in agreement with recent reports.⁵⁸ Otsuka *et al.* hypothesized that metallic promoters could enhance the MPO reaction rate by a reverse spillover mechanism.⁶⁰ This catalytic effect could explain the rate improvement observed in this work by Co exsolution. The precise mechanism for exsolved Co-mediated methane activation elucidated through kinetic analysis and operando techniques is an on-going topic for future work.

Next, we assessed the fuel product selectivity, exemplified by the selectivity toward CO production, S_{CO} , (values for H₂ selectivity would lie in the same range²). Figure 4b depicts that exLSCC has the highest S_{CO} , *viz.*, 94% selectivity, whereas LSCC and ceria showed 70 and 88%, respectively. In addition, selectivity values for exLSCC were higher than recently reported values for La_{0.5}Ca_{0.4}Ni_{0.2}Ti_{0.8}O_{3- γ} decorated with exsolved Ni nanoparticles ($S_{\text{CO}} \approx 80\%$).⁶¹ Deviations from total selectivity values are indicative of the formation of oxygenated species coming from the combustion reaction, eq 2. This result is shown in Figure S3, Supporting Information, in which the H₂, CO, CO₂, and H₂O gas production curves are plotted for each material. It can be observed that right after CH₄ injection, LSCC produced a considerably higher amount of H₂O and CO₂ when compared to exLSCC, Figure S3. This phenomenon is related to the combustion of CH₄ with readily available surface oxygen.³ As shown in the O 1s XPS spectra of Figure S2, the exsolution treatment induced a higher amount of oxygen vacancies at the surface of exLSCC. Thus, the low amount of readily available oxygen at the surface of exLSCC decreased the tendency to form oxygenated molecules (CO₂ and H₂O) and thereby enhances the selectivity toward syngas.²⁵

Additional key metrics for the MPO reaction, such as total H₂ production, CO production rates, and H₂/CO ratios, are also depicted in Figure 4b. The CO peak production rate values showed a similar trend as for the H₂ production shown in Figure 4a, with exLSCC exhibiting the fastest syngas production kinetics. Regarding the total H₂ production, ceria exhibited the highest values of the three materials, 46.4 mL g⁻¹, whereas exLSCC showed a production rate of 36.9 mL g⁻¹. The higher H₂ production observed for ceria is related to the slowest but constant H₂ production profile compared to the

perovskites, Figure 4a. Namely, after 2 min under CH₄ exposure, exLSCC reached 82% of its total H₂ production, whereas ceria reached just 40%, illustrating the faster MPO kinetics of exLSCC. This performance directly affects the overall CH₄ conversion, that is, considering just the first minute of reduction, exLSCC exhibits a higher conversion than ceria, 45.9 versus 40.3%, respectively; however, ceria exhibits a higher total conversion for the entire MPO half cycle, 16.7 and 22.2%, respectively, Figure S3 in the Supporting Information. Nevertheless, the conditions used here were not designed to favor methane conversion, which could be optimized by, for example, increasing the temperature, using different CH₄ concentrations² or shorter CH₄ injections.

Figure 4b also shows the H₂/CO molar ratio for the three materials tested. Ideally, the H₂/CO ratio should lie around 2, as described by the stoichiometry of eq 1. Deviations from this value generally arise from CH₄ cracking, which forms solid carbon and H₂, resulting in a ratio of H₂/CO > 2. The three materials exhibited values around 2, which is a good indication that under these conditions, carbon deposition is avoided, showing improved resistance against coking that Ni-promoted perovskites used for this same type of reaction, as recently reported by Otto *et al.*⁵²

2.3. CO₂-Splitting Performance. Now, we turn to the analysis of the CO₂-splitting half cycle. Figure 5 depicts the CO production rate curves at 900 °C and with 16 vol % CO₂ injection. It shows that all the materials exhibit the capacity to split CO₂. Interestingly, exLSCC showed a higher CO peak production rate than LSCC, *viz.* 96.5 and 55.4 mL min⁻¹ g⁻¹, respectively. This twofold improvement reveals the positive impact that the exsolved nanoparticles have on accelerating the CO₂-splitting kinetics of perovskite oxides. Previous reports have shown improved H₂O-splitting kinetics for Rh-decorated CeO₂ compared to bare CeO₂ at temperatures 800–1000 °C, ascribed to enhanced surface reaction kinetics caused by the metallic catalyst.⁶² Furthermore, exLSCC also exhibits faster CO production rate than CeO₂, 96.5 and 70.6 mL min⁻¹ g⁻¹, respectively, which is a material well known for its rapid CO₂-splitting kinetics.⁶³ To put these values into perspective, Li *et al.* have recently reported 168 mL min⁻¹ g⁻¹ with 5% Ni supported on CeO₂-TiO₂.¹⁸ In this work, however, a stream of 100% CO₂ was used, whereas we utilized only 16% CO₂. Thus, it is expected that using 100% CO₂, the peak rate values of exLSCC will be further improved because the higher the p_{CO_2} , the faster the CO₂-splitting rates.⁶⁴

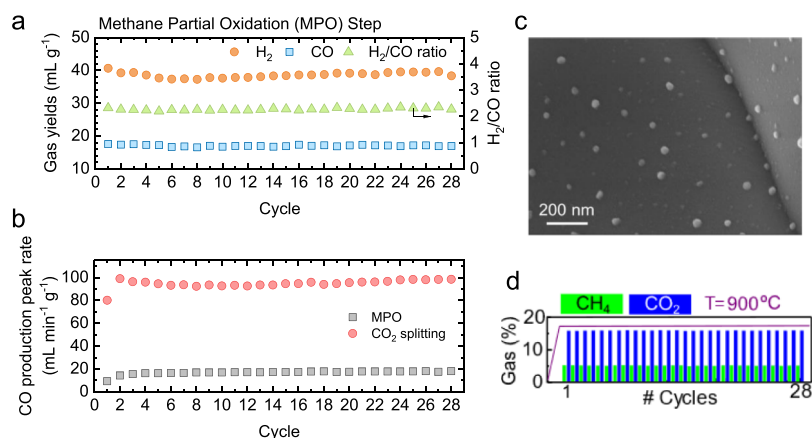


Figure 6. (a) CO, H₂ total production, and H₂/CO ratio obtained during the MPO half cycle of a 28-cycle chemical looping methane reforming test, performed to the LSCC perovskite after exsolution (exLSCC). (b) Comparison of the peak CO production rates for both the MPO and CO₂-splitting half cycles, during the 28-cycle test at 900 °C, using 5% CH₄ and 16% CO₂ 5 min pulses. (c) SEM image of the exsolved LSCC perovskite (exLSCC) after the 28-cycle test depicted in (d).

The total amount of produced CO from the CO₂-splitting half cycle was determined for each material. Results show that exLSCC produced 31.3 mL g⁻¹, whereas ceria and LSCC produced 27.6 and 24.6 mL g⁻¹, respectively. CO₂ conversion values were 3.3, 2.6, and 2.9% for exLSCC, LSCC, and Ceria, respectively. However, because of the fast CO₂-splitting rates, when determining the conversion for just the first minute of CO₂ exposure, values were 13.1, 10.0, and 14.1%, respectively. These results together with the syngas production rates, Figure 4, indicate that it would be more efficient to perform the chemical looping reforming with shorter gas injections, for example, 2 min CH₄ and 1 min CO₂ pulses, which will be especially beneficial for exLSCC because it presents the fastest reaction rates. Overall, shorter gas injections would optimize the process, increasing CH₄ and CO₂ conversions and increasing the process energy efficiency, as recently demonstrated by Warren *et al.*²¹ In addition, our CO₂-splitting experiments were not aimed at high CO₂ conversions because lowering CO₂ vol % could have been further used to increase the CO₂-splitting conversion. However, this increase will come at the expense of slower CO₂-splitting rates because the higher the pCO₂, the higher the reaction rate is.⁶⁴

The higher amount of fuel produced by exLSCC compared to LSCC is because of a higher reducibility of the former ascribed to the presence of the exsolved nanoparticles. This fact was recently pointed out by Hosseini *et al.* who reported an increase in the reducibility of Ca₂Fe₂O₅ induced by Cu nanoparticles.⁵¹ Additionally, catalytically active surfaces increase the ionic conductivity driven by surface oxygen removal, as explained by Zhu *et al.*,³⁰ which will directly impact the rate at which oxygen vacancies are replenished with oxygen coming from CO₂. In addition, other effects such as faster CO₂ adsorption and dissociation at the surface catalyzed by the presence of the Co nanoparticles could also play a role in the kinetic improvement caused by exsolution functionalization. The increased rate of O²⁻ transport through the bulk caused by the nanoparticle decoration could also affect the amount of oxygen vacancies created during the reduction step. According to our results, both the syngas produced during the MPO, Figure 4, and the CO produced during the CO₂-splitting reaction, Figure 5, indicate that exLSCC achieved a higher degree of nonstoichiometry in the reduction step, δ ; thus, higher amounts of fuel are produced for both steps. These

results point toward an additional impact on the surface functionalization in increasing the amount of oxygen vacancies, which are higher for exLSCC than for LSCC.

In summary, the results show how LSCC surface functionalization by means of Co exsolution nanoparticle decoration improved the MPO reaction, with a high selectivity toward syngas production, an S_{CO} of 94%, exhibiting two and three times faster fuel production rates if compared with the bare perovskite and ceria, respectively. In terms of syngas production rate, the improvement is also remarkable when compared with existing literature. For instance, Zhang *et al.* reported a H₂ peak production of 10.8 mL min⁻¹ g⁻¹ (8.03 mmol s⁻¹ kg⁻¹) using a perovskite Sr₃Fe₂O_{7- δ} -Ca_{0.5}Mn_{0.5}O nanocomposite,⁶⁵ which is about four times less than our reported values, Figure 4a. In terms of total fuel production, comparison with existing literature could be misleading because reported values depend on the gas injection times and material reaction kinetics. For instance, Chen *et al.*⁶⁶ reported a H₂ productivity of about ca. 15 μ mol g⁻¹, with CeO₂/LaFeO₃ composites at 850 °C and 10 min CH₄ injections, which is about 0.34 mL g⁻¹, that is, 2 orders of magnitude lower than the values reported herein, Figure 4b. On the other hand, Sastre *et al.* reported a H₂ production of 286.7 mL g⁻¹ (12.8 mmol g⁻¹), which is almost 1 order of magnitude higher than the values reported here, but also conducted with longer CH₄ injections of 30 min.²⁶

Remarkably, exLSCC CO₂-splitting performance is also improved with respect to state-of-the-art ceria, both in terms of kinetics and fuel production. Literature reports on perovskites for chemical looping reforming coupled with CO₂ are quite scarce,⁶¹ and few of them report CO rate production values. In this sense, Zhang *et al.* reports CO production rate values of 30.1 mL min⁻¹ g⁻¹ (22 mmol kg⁻¹ s⁻¹) from the CO₂-splitting reaction,⁶⁵ which is about three times less than the CO production rates for exLSCC, Figure 5a.

In summary, our results point toward the beneficial impact on nanoparticle exsolution in the entire chemical looping reforming process. In addition, the promising catalytic functionalities exhibited by exLSCC would merit a future study utilizing lower temperatures, which will be especially interesting for upgrading industrial waste heat.⁵ However, lowering the working temperature could result in lower CH₄ conversions⁵ and a decrease in the oxygen exchange capacity

because the creation of oxygen vacancies is favored at high temperatures. This latter fact could also imply a lower activity of the materials for the CO₂-splitting reaction step.

2.4. Chemical Looping Reforming Longevity Test and Nanoparticle Stability. In order to elucidate the stability of the exsolved nanoparticles and the fuel production behavior during prolonged cycling at high temperatures, exLSCC was subjected to 28 chemical loops at 900 °C. Figure 6a shows the H₂ and CO yields corresponding to the MPO half cycle. Production of both gases was stable during the entire multicycle test, with average fuel production values of $38.6 \pm 0.8 \text{ mL}_{\text{H}_2} \text{ g}^{-1}$ and $17.05 \pm 0.2 \text{ mL}_{\text{CO}} \text{ g}^{-1}$, resulting in a H₂/CO ratio of *ca.* 2.2. Both results match well with the production values obtained in the initial screening, see Figure 4. Similarly, the CO production rate, Figure 6b, quantified for the MPO and the CO₂-splitting half cycles exhibited constant values over the 28 cycles for both reactions, pointing toward a high catalytic stability of the exsolved nanoparticles. In order to confirm the microstructural stability, SEM and TEM–EDS analyses were performed on the exLSCC material after the 28 chemical loops, Figures 6c and S4. After such a prolonged redox cycling, the exsolution-functionalized perovskite shows the presence of exsolved nanoparticles with an average particle size of $37 \pm 7 \text{ nm}$, which indicates a minor particle size increase with respect to the pristine exsolved nanoparticles ($32 \pm 7 \text{ nm}$). The fact that the exsolved particles remain anchored and with such a little size variation reveals the prospect of the exsolution method. It is of interest in future work to test it over more prolonged cycling, while optimizing the times for the MPO and CO₂-splitting steps to elucidate which step affects the particle size the most. TEM–EDS confirms that these nanoparticles are solely formed by cobalt (see the Supporting Information, Figure S4, for further details). It is known that, dependent on the chemistry in exsolution-treated perovskite cermet structures, some exsolved nanoparticles may also dissolve back to the perovskite lattice. To test specifically whether the cobalt nanoparticle prevails after oxidation under CO₂, we selected the TEM and SEM analyses to be carried out after the last oxidation step. This confirms that once the exsolved cobalt nanoparticles have formed on the surface of the LSCC in the initial processing of the material in a hydrogen reduction step carried out at 900 °C, these nanoparticles remain stable for the tested methane redox MPO–CO₂-splitting cycles.

This result proves that under certain oxidative conditions, exsolution might not be entirely reversible, preserving its catalytic activity for both the reduction and the oxidation steps. Previous studies have reported reversible re-oxidation that employs harsher oxidative conditions, for example, air for 20 h,^{67,68} than those in our current work, 16 vol % CO₂ for just 5 min, which might not be enough for driving the redissolution of the anchored particles back in the perovskite backbone, as recently reported by Hosseini *et al.*⁵¹ Nonetheless, the fact that under the experimental conditions used in this work, the exsolution-promoted perovskite maintained the cobalt nanoparticles for both the reduction and oxidation steps is by all ends positive because the presence of the anchored nanoparticles exhibited catalytic improvements for both reactions.

3. CONCLUSIONS

In this work, we fabricated Co nanoparticles of around 30 nm, anchored to the redox-active LSCC perovskite, as corroborated

by TEM and XPS, which exhibited stable syngas production over 28 chemical loops, with remarkable nanoparticle stability and dispersion after thermochemical cycling at high temperatures. Furthermore, the exsolution-promoted perovskite exhibited improved reaction rate performance for both the MPO and CO₂-splitting half cycles, outperforming the bare perovskite. Namely, Co nanoparticle exsolution induced a twofold faster H₂ production rate, higher selectivity toward syngas production, and *ca.* twofold faster CO₂-splitting rates. Additionally, when compared with CeO₂, a well-known reference material in the field of thermochemical cycles, the exsolution-promoted perovskite achieved threefold faster MPO rates and a maximum CO₂-splitting peak rate of *ca.* 100 mL min⁻¹ g⁻¹ at 900 °C (compared to 70 mL min⁻¹ g⁻¹ for CeO₂). In addition, it was also confirmed that oxidation under CO₂ does not redissolve the nanoparticles into the perovskite backbone, which helps improving its catalytic activity for each reaction step of this cyclic process.

In summary, this paper corroborates that surface functionalization *via* nanoparticle anchoring represents a facile route for generating highly dispersed metallic nanoparticles, preventing particle agglomeration, which guarantees high chemical stability over prolonged cycling at high temperatures. The results reported here open the path for further optimization and investigation of other exsolution-promoted oxide compositions that could exhibit improved catalytic activity in thermochemical production of fuels or added value chemicals.

4. EXPERIMENTAL PROCEDURES

4.1. Material Preparation. LSCC was synthesized using a modified version of the Pechini method. Citric acid (Sigma-Aldrich, ≥99%) together with stoichiometric amounts of nitrate precursors, namely, La(NO₃)₃·6H₂O (Sigma-Aldrich, ≥99.99%), Sr(NO₃)₂ (Fluka Analytical, ≥99%), Cr(NO₃)₂·9H₂O (Sigma-Aldrich, ≥97%), and Co(NO₃)₂·4H₂O (Sigma Aldrich, ≥97%), were dissolved in deionized water at room temperature in a 3:2 molar ratio. Afterward, the aqueous solution was heated to 80 °C under constant stirring, followed by the addition of ethylene glycol (Fluka Analytical, ≥98%) in a 2/3 weight ratio. Continuing the stirring and maintaining the temperature at 80 °C, water was evaporated until a gel was formed. The gel was then dried on a heating plate at 200 °C for 2 h followed by calcination for 1 h at 400 °C. The calcined gel was ground to fine powders in an agate mortar and heat-treated in an alumina crucible at 1400 °C for 5 h. After that, part of the powder was reduced in a tube furnace at 900 °C for 10 h, under a constant flow of 5% H₂, balanced with Ar (200 mL min⁻¹ total flow), in order to drive the exsolution. Commercial CeO₂ (Sigma-Aldrich, nanopowder with an average grain size of 50 nm, 99.95% purity) was used as received.

4.2. Material Physicochemical Characterization. XRD data were collected with a Panalytical X'Pert PRO MPD diffractometer. Cu K α radiation ($\lambda = 1.54178 \text{ \AA}$) produced with an extraction voltage of 45 kV at 40 mA current was used to scan the samples in a Bragg–Brentano geometry in the range of $20^\circ < 2\theta < 120^\circ$ with a spinning speed of 60 rpm⁻¹, a step width of 0.017°, and an irradiation time of 3 s. Unit cell parameters were determined by Rietveld refinement using Panalytical HighScore Plus software, considering a rhombohedral perovskite model structure and fitting the experimental data with a Pseudo Voigt function. For XRD with *in situ* heating, the perovskite powders were placed in an Anton Paar HTK 1200N high-temperature oven chamber and heated up to 950 °C for 260 min, always under a 5 vol % H₂/Ar flow of 100 mL min⁻¹. During the heating stage, patterns were collected at temperature intervals of 50 °C. During the isothermal stage, patterns were recorded each 20 min. Microstructure and particle morphology were assessed on a Zeiss Merlin high-resolution scanning electron microscope. An acceleration voltage of 7 kV was used for all images. The exsolved nanoparticle size distribution

was determined by image analyses of *ca.* 200 nanoparticles with software ImageJ.⁶⁹ STEM and EDS were performed on a JEOL JEM 2200FS STEM/TEM microscope at an acceleration voltage of 200 kV equipped with a CEOS probe corrector (Heidelberg, Germany) to provide a nominal resolution of ~ 0.07 nm. A Bruker AXS silicon drift detector was used for all EDS elemental analysis. HR-TEM was performed on an aberration-corrected FEI Titan S 80–300 STEM/TEM microscope equipped with a Gatan OneView camera at an acceleration voltage of 300 kV. All samples were prepared for HR-TEM by drop-casting 8 μL of the as-prepared aqueous dispersions of powders onto lacey carbon-coated copper TEM grids. XPS was performed on a Thermo K-Alpha ZPS system with a spot size of 400 μm and a resolution of 0.1 eV. All XPS spectra were analyzed using Advantage 5.959, a software package provided by Thermo Scientific.

4.3. Chemical Looping Reforming Tests. Chemical looping reforming of methane was evaluated in a high-temperature fixed-bed reactor connected to a Raman laser gas analyzer (Atmospheric Recovery, Inc), as described elsewhere.⁷⁰ Figure S5 illustrates the experimental reactor setup. About 0.25 g of oxide material was used for each test. Reactions were carried out under a reduction/oxidation cycling program at 900 °C. For the first half cycle, MPO was performed by injecting 5 vol % CH_4 (15 mL min^{-1} , balanced with Ar, 99.999% purity, Airgas, for a total flow of 300 mL min^{-1}). Subsequently, CO_2 splitting was conducted by injecting 16 vol % CO_2 (99.998% purity, Airgas, balanced with Ar for a total flow of 300 mL min^{-1}). After each reaction, Ar (300 mL min^{-1}) was injected to purge the reactor. CO selectivity, S_{CO} , was calculated through eq 6, where \dot{n}_{CO} and \dot{n}_{CO_2} are the molar flow rates of CO and CO_2 , respectively.

$$S_{\text{CO}} = \frac{\dot{n}_{\text{CO}}}{\dot{n}_{\text{CO}} + \dot{n}_{\text{CO}_2}} \quad (6)$$

■ ASSOCIATED CONTENT

Supporting Information

The Supporting Information is available free of charge at <https://pubs.acs.org/doi/10.1021/acsaem.0c00249>.

Rietveld refinements, XPS spectra before and after exsolution, gas production curves and conversion for the MPO reaction, HAADF-STEM analysis after cycling, and schematic of the experimental reactor setup (PDF)

■ AUTHOR INFORMATION

Corresponding Author

Jennifer L. M. Rupp – *Electrochemical Materials Laboratory, Department of Materials Science and Engineering and Electrochemical Materials Laboratory, Department of Electrical Engineering and Computer Science, Massachusetts Institute of Technology, 02139 Cambridge, Massachusetts, United States;* orcid.org/0000-0001-7160-0108; Email: jrupp@mit.edu

Authors

Alfonso J. Carrillo – *Electrochemical Materials Laboratory, Department of Materials Science and Engineering, Massachusetts Institute of Technology, 02139 Cambridge, Massachusetts, United States*

Kun Joong Kim – *Electrochemical Materials Laboratory, Department of Materials Science and Engineering, Massachusetts Institute of Technology, 02139 Cambridge, Massachusetts, United States*

Zachary D. Hood – *Electrochemical Materials Laboratory, Department of Materials Science and Engineering, Massachusetts Institute of Technology, 02139 Cambridge, Massachusetts, United States;* orcid.org/0000-0002-5720-4392

Alexander H. Bork – *Electrochemical Materials Group, Department of Materials Science, ETH Zurich, 8093 Zürich, Switzerland*

Complete contact information is available at: <https://pubs.acs.org/doi/10.1021/acsaem.0c00249>

Notes

The authors declare no competing financial interest.

■ ACKNOWLEDGMENTS

The authors thank the support of ENI and the MIT Energy Initiative. A portion of this research was conducted at the Center for Nanophase Materials Sciences, which is a DOE Office of Science User Facility. Z.D.H. was supported by a Fellowship through the National Science Foundation (DGE-1650044). This work made use of the MRSEC Shared Experimental Facilities at MIT, supported by the National Science Foundation under award number DMR-14-19807.

■ REFERENCES

- (1) Zhu, X.; Donat, F.; Imtiaz, Q.; Müller, C. R.; Li, F. Chemical Looping Beyond Combustion – A Perspective. *Energy Environ. Sci.* **2020**, *13*, 772.
- (2) Krenzke, P. T.; Fosheim, J. R.; Zheng, J.; Davidson, J. H. Synthesis Gas Production via the Solar Partial Oxidation of Methane-Ceria Redox Cycle: Conversion, Selectivity, and Efficiency. *Int. J. Hydrogen Energy* **2016**, *41*, 12799–12811.
- (3) Krenzke, P. T.; Fosheim, J. R.; Davidson, J. H. Solar Fuels via Chemical-Looping Reforming. *Sol. Energy* **2017**, *156*, 48–72.
- (4) Agrafiotis, C.; Von Storch, H.; Roeb, M.; Sattler, C. Solar Thermal Reforming of Methane Feedstocks for Hydrogen and Syngas Production - A Review. *Renewable Sustainable Energy Rev.* **2014**, *29*, 656–682.
- (5) Yusuf, S.; Haribal, V.; Jackson, D.; Neal, L.; Li, F. Mixed Iron-Manganese Oxides as Redox Catalysts for Chemical Looping–Oxidative Dehydrogenation of Ethane with Tailorable Heat of Reactions. *Appl. Catal., B* **2019**, *257*, 117885.
- (6) Steinfeld, A.; Kuhn, P.; Karni, J. High-Temperature Solar Thermochemistry: Production of Iron and Synthesis Gas by Fe_3O_4 -Reduction with Methane. *Energy* **1993**, *18*, 239–249.
- (7) Zeng, L.; Cheng, Z.; Fan, J. A.; Fan, L.-S.; Gong, J. Metal Oxide Redox Chemistry for Chemical Looping Processes. *Nat. Rev. Chem.* **2018**, *2*, 349–364.
- (8) Chuayboon, S.; Abanades, S.; Rodat, S. Stepwise Solar Methane Reforming and Water-Splitting via Lattice Oxygen Transfer in Iron and Cerium Oxides. *Energy Technol.* **2019**, 1900415.
- (9) Tang, M.; Liu, K.; Roddick, D. M.; Fan, M. Enhanced Lattice Oxygen Reactivity over $\text{Fe}_2\text{O}_3/\text{Al}_2\text{O}_3$ redox Catalyst for Chemical-Looping Dry (CO_2) Reforming of CH_4 : Synergistic La-Ce Effect. *J. Catal.* **2018**, *368*, 38–52.
- (10) Gao, X.; Liu, G.; Zhu, Y.; Kreider, P.; Bayon, A.; Gengenbach, T.; Lu, T.; Liu, Y.; Hinkley, J.; Lipiński, W.; Tricoli, A. Earth-Abundant Transition Metal Oxides with Extraordinary Reversible Oxygen Exchange Capacity for Efficient Thermochemical Synthesis of Solar Fuels. *Nano Energy* **2018**, *50*, 347–358.
- (11) Gao, X.; Di Bernardo, I.; Kreider, P.; Tran-Phu, T.; Cai, X.; Wang, N.; Zhu, Y.; Venkataraman, M. B.; Lipton-Duffin, J.; Bayon, A.; Lipiński, W.; Tricoli, A. Lattice Expansion in Optimally Doped Manganese Oxide: An Effective Structural Parameter for Enhanced Thermochemical Water Splitting. *ACS Catal.* **2019**, *9*, 9880–9890.
- (12) Krenzke, P. T.; Davidson, J. H. Thermodynamic Analysis of Syngas Production via the Solar Thermochemical Cerium Oxide Redox Cycle with Methane-Driven Reduction. *Energy Fuels* **2014**, *28*, 4088–4095.
- (13) Krenzke, P. T.; Davidson, J. H. On the Efficiency of Solar H_2 and CO Production via the Thermochemical Cerium Oxide Redox

Cycle: The Option of Inert-Swept Reduction. *Energy Fuels* **2015**, *29*, 1045.

(14) Gao, X.; Vidal, A.; Bayon, A.; Bader, R.; Hinkley, J.; Lipiński, W.; Tricoli, A. Efficient Ceria Nanostructures for Enhanced Solar Fuel Production via High-Temperature Thermochemical Redox Cycles. *J. Mater. Chem. A* **2016**, *4*, 9614–9624.

(15) Li, K.; Wang, H.; Wei, Y.; Yan, D. Syngas Production from Methane and Air via a Redox Process Using Ce-Fe Mixed Oxides as Oxygen Carriers. *Appl. Catal., B* **2010**, *97*, 361–372.

(16) Warren, K. J.; Scheffe, J. R. Kinetic Insights into the Reduction of Ceria Facilitated via the Partial Oxidation of Methane. *Mater. Today Energy* **2018**, *9*, 39–48.

(17) Fosheim, J. R.; Hathaway, B. J.; Davidson, J. H. High Efficiency Solar Chemical-Looping Methane Reforming with Ceria in a Fixed-Bed Reactor. *Energy* **2019**, *169*, 597–612.

(18) Ruan, C.; Huang, Z.-Q.; Lin, J.; Li, L.; Liu, X.; Tian, M.; Huang, C.; Chang, C.-R.; Li, J.; Wang, X. Synergy of the Catalytic Activation on Ni and the CeO₂-TiO₂/Ce₂Ti₂O₇ Stoichiometric Redox Cycle for Dramatically Enhanced Solar Fuel Production. *Energy Environ. Sci.* **2019**, *12*, 767–779.

(19) Warren, K. J.; Reim, J.; Randhir, K.; Greek, B.; Carrillo, R.; Hahn, D. W.; Scheffe, J. R. Theoretical and Experimental Investigation of Solar Methane Reforming through the Non-stoichiometric Ceria Redox Cycle. *Energy Technol.* **2017**, *5*, 2138–2149.

(20) Welte, M.; Warren, K.; Scheffe, J. R.; Steinfeld, A. Combined Ceria Reduction and Methane Reforming in a Solar-Driven Particle-Transport Reactor. *Ind. Eng. Chem. Res.* **2017**, *56*, 10300–10308.

(21) Warren, K. J.; Carrillo, R. J.; Greek, B.; Hill, C. M.; Scheffe, J. R. Solar Reactor Demonstration of Efficient and Selective Syngas Production via Chemical Looping Dry Reforming of Methane over Ceria. *Energy Technol.* **2020**, 2000053.

(22) Marxer, D.; Furler, P.; Takacs, M.; Steinfeld, A. Solar Thermochemical Splitting of CO₂ into Separate Streams of CO and O₂ with High Selectivity, Stability, Conversion, and Efficiency. *Energy Environ. Sci.* **2017**, *10*, 1142–1149.

(23) Ribeiro, M. C.; Jacobs, G.; Pendyala, R.; Davis, B. H.; Cronauer, D. C.; Kropf, A. J.; Marshall, C. L. Fischer–Tropsch Synthesis: Influence of Mn on the Carburization Rates and Activities of Fe-Based Catalysts by TPR-EXAFS/XANES and Catalyst Testing. *J. Phys. Chem. C* **2011**, *115*, 4783–4792.

(24) Neal, L. M.; Shafiearhood, A.; Li, F. Dynamic Methane Partial Oxidation Using a Fe₂O₃@La_{0.8}Sr_{0.2}FeO_{3-δ} Core-Shell Redox Catalyst in the Absence of Gaseous Oxygen. *ACS Catal.* **2014**, *4*, 3560–3569.

(25) Shafiearhood, A.; Hamill, J. C.; Neal, L. M.; Li, F. Methane Partial Oxidation Using FeO_x@La_{0.8}Sr_{0.2}FeO_{3-δ} Core-Shell Catalyst-Transient Pulse Studies. *Phys. Chem. Chem. Phys.* **2015**, *17*, 31297–31307.

(26) Sastre, D.; Serrano, D. P.; Pizarro, P.; Coronado, J. M. Chemical Insights on the Activity of La_{1-x}Sr_xFeO₃ Perovskites for Chemical Looping Reforming of Methane Coupled with CO₂-Splitting. *J. CO₂ Util.* **2019**, *31*, 16–26.

(27) Shafiearhood, A.; Zhang, J.; Neal, L. M.; Li, F. Rh-Promoted Mixed Oxides for “Low-Temperature” Methane Partial Oxidation in the Absence of Gaseous Oxidants. *J. Mater. Chem. A* **2017**, *5*, 11930–11939.

(28) Haribal, V. P.; He, F.; Mishra, A.; Li, F. Iron-Doped BaMnO₃ for Hybrid Water Splitting and Syngas Generation. *ChemSusChem* **2017**, *10*, 3402–3408.

(29) Mishra, A.; Galinsky, N.; He, F.; Santiso, E. E.; Li, F. Perovskite-Structured AM_nB_{1-x}O₃ (A = Ca or Ba; B = Fe or Ni) Redox Catalysts for Partial Oxidation of Methane. *Catal. Sci. Technol.* **2016**, *6*, 4535–4544.

(30) Zhu, X.; Li, K.; Neal, L.; Li, F. Perovskites as Geo-Inspired Oxygen Storage Materials for Chemical Looping and Three-Way Catalysis - A Perspective. *ACS Catal.* **2018**, *8*, 8213–8236.

(31) He, F.; Li, F. Perovskite Promoted Iron Oxide for Hybrid Water-Splitting and Syngas Generation with Exceptional Conversion. *Energy Environ. Sci.* **2015**, *8*, 535–539.

(32) Mishra, A.; Li, F. Chemical Looping at the Nanoscale — Challenges and Opportunities. *Curr. Opin. Chem. Eng.* **2018**, *20*, 143–150.

(33) Geus, J. W.; van Dillen, A. J. Preparation of Supported Catalysts by Deposition-Precipitation. *Handbook of Heterogeneous Catalysis*; Wiley-VCH Verlag GmbH & Co. KGaA: Weinheim, Germany, 2008; pp 428–467.

(34) Jiang, S. P.; Ye, Y.; He, T.; Ho, S. B. Nanostructured Palladium-La_{0.75}Sr_{0.25}Cr_{0.5}Mn_{0.5}O₃/Y₂O₃-ZrO₂ Composite Anodes for Direct Methane and Ethanol Solid Oxide Fuel Cells. *J. Power Sources* **2008**, *185*, 179–182.

(35) Hansen, T. W.; DeLaRiva, A. T.; Challa, S. R.; Datye, A. K. Sintering of Catalytic Nanoparticles: Particle Migration or Ostwald Ripening? *Acc. Chem. Res.* **2013**, *46*, 1720–1730.

(36) Han, H.; Park, J.; Nam, S. Y.; Kim, K. J.; Choi, G. M.; Parkin, S. S. P.; Jang, H. M.; Irvine, J. T. S. Lattice Strain-Enhanced Exsolution of Nanoparticles in Thin Films. *Nat. Commun.* **2019**, *10*, 1471.

(37) Jo, Y.-R.; Koo, B.; Seo, M.-J.; Kim, J. K.; Lee, S.; Kim, K.; Han, J. W.; Jung, W.; Kim, B.-J. Growth Kinetics of Individual Co Particles Ex-Solved on SrTi_{0.75}Co_{0.25}O_{3-δ} Polycrystalline Perovskite Thin Films. *J. Am. Chem. Soc.* **2019**, *141*, 6690–6697.

(38) Kobsiriphat, W.; Madsen, B. D.; Wang, Y.; Shah, M.; Marks, L. D.; Barnett, S. a. Nickel- and Ruthenium-Doped Lanthanum Chromite Anodes: Effects of Nanoscale Metal Precipitation on Solid Oxide Fuel Cell Performance. *J. Electrochem. Soc.* **2010**, *157*, B279.

(39) Zenou, V. Y.; Fowler, D. E.; Gautier, R.; Barnett, S. A.; Poeppelmeier, K. R.; Marks, L. D. Redox and Phase Behavior of Pd-Substituted (La,Sr)CrO₃ Perovskite Solid Oxide Fuel Cell Anodes. *Solid State Ionics* **2016**, *296*, 90–105.

(40) Tanaka, H.; Taniguchi, M.; Uenishi, M.; Kajita, N.; Tan, I.; Nishihata, Y.; Mizuki, J. i.; Narita, K.; Kimura, M.; Kaneko, K. Self-Regenerating Rh- and Pt-Based Perovskite Catalysts for Automotive Emissions Control. *Angew. Chem.* **2006**, *118*, 6144–6148.

(41) Lai, K.-Y.; Manthiram, A. Evolution of Exsolved Nanoparticles on a Perovskite Oxide Surface during a Redox Process. *Chem. Mater.* **2018**, *30*, 2838–2847.

(42) Neagu, D.; Tsekouras, G.; Miller, D. N.; Ménard, H.; Irvine, J. T. S. In Situ Growth of Nanoparticles through Control of Non-Stoichiometry. *Nat. Chem.* **2013**, *5*, 916–923.

(43) Papargyriou, D.; Irvine, J. T. S. Nickel Nanocatalyst Exsolution from (La,Sr) (Cr,M,Ni)O₃ (M=Mn,Fe) Perovskites for the Fuel Oxidation Layer of Oxygen Transport Membranes. *Solid State Ionics* **2016**, *288*, 120–123.

(44) Oh, T.-S.; Rahani, E. K.; Neagu, D.; Irvine, J. T. S.; Shenoy, V. B.; Gorte, R. J.; Vohs, J. M. Evidence and Model for Strain-Driven Release of Metal Nanocatalysts from Perovskites during Exsolution. *J. Phys. Chem. Lett.* **2015**, *6*, 5106–5110.

(45) Liu, S.; Liu, Q.; Luo, J.-L. Highly Stable and Efficient Catalyst with in Situ Exsolved Fe-Ni Alloy Nanospheres Socketed on an Oxygen Deficient Perovskite for Direct CO₂ Electrolysis. *ACS Catal.* **2016**, *6*, 6219–6228.

(46) Zhu, T.; Troiani, H. E.; Mogni, L. V.; Han, M.; Barnett, S. A. Ni-Substituted Sr(Ti,Fe)O₃ SOFC Anodes: Achieving High Performance via Metal Alloy Nanoparticle Exsolution. *Joule* **2018**, *2*, 478–496.

(47) Neagu, D.; Papaioannou, E. I.; Ramli, W. K. W.; Miller, D. N.; Murdoch, B. J.; Ménard, H.; Umar, A.; Barlow, A. J.; Cumpson, P. J.; Irvine, J. T. S.; Metcalfe, I. S. Demonstration of Chemistry at a Point through Restructuring and Catalytic Activation at Anchored Nanoparticles. *Nat. Commun.* **2017**, *8*, 1855.

(48) Park, S.; Kim, Y.; Noh, Y.; Kim, T.; Han, H.; Yoon, W.; Choi, J.; Yi, S.; Lee, W.; Kim, W. B. Sulfur-Tolerant Cathode Catalyst Fabricated with in Situ Exsolved CoNi Alloy Nanoparticles Anchored on a Ruddlesden-Popper Support for CO₂ Electrolysis. *J. Mater. Chem. A* **2020**, *8*, 138.

(49) Irvine, J. T. S.; Neagu, D.; Verbraeken, M. C.; Chatzichristodoulou, C.; Graves, C.; Mogensen, M. B. Evolution of

the Electrochemical Interface in High-Temperature Fuel Cells and Electrolysers. *Nat. Energy* **2016**, *1*, 15014.

(50) Neagu, D.; Oh, T. S.; Miller, D. N.; Menard, H.; Bukhari, S. M.; Gamble, S. R.; Gorte, R. J.; Vohs, J. M.; Irvine, J. T. Nano-Socketed Nickel Particles with Enhanced Coking Resistance Grown in Situ by Redox Exsolution. *Nat. Commun.* **2015**, *6*, 8120.

(51) Hosseini, D.; Donat, F.; Abdala, P. M.; Kim, S. M.; Kierzkowska, A. M.; Müller, C. R. Reversible Exsolution of Dopant Improves the Performance of $\text{Ca}_2\text{Fe}_2\text{O}_5$ for Chemical Looping Hydrogen Production. *ACS Appl. Mater. Interfaces* **2019**, *11*, 18276–18284.

(52) Otto, S.-K.; Kousi, K.; Neagu, D.; Bekris, L.; Janek, J.; Metcalfe, I. S. Exsolved Nickel Nanoparticles Acting as Oxygen Storage Reservoirs and Active Sites for Redox CH_4 Conversion. *ACS Appl. Energy Mater.* **2019**, *2*, 7288–7298.

(53) Kousi, K.; Neagu, D.; Bekris, L.; Papaioannou, E. I.; Metcalfe, I. S. Endogenous Nanoparticles Strain Perovskite Host Lattice Providing Oxygen Capacity and Driving Oxygen Exchange and CH_4 Conversion to Syngas. *Angew. Chem., Int. Ed.* **2020**, *59*, 2510–2519.

(54) Dimitrakopoulos, G.; Ghoniem, A. F.; Yildiz, B. In Situ Catalyst Exsolution on Perovskite Oxides for the Production of CO and Synthesis Gas in Ceramic Membrane Reactors. *Sustain. Energy Fuels* **2019**, *3*, 2347–2355.

(55) Bork, A. H.; Kubicek, M.; Struzik, M.; Rupp, J. L. M. Perovskite $\text{La}_{0.6}\text{Sr}_{0.4}\text{Cr}_{1-x}\text{Co}_x\text{O}_{3-\delta}$ Solid Solutions for Solar-Thermochemical Fuel Production: Strategies to Lower the Operation Temperature. *J. Mater. Chem. A* **2015**, *3*, 15546–15557.

(56) Budiman, A. W.; Song, S.-H.; Chang, T.-S.; Shin, C.-H.; Choi, M.-J. Dry Reforming of Methane Over Cobalt Catalysts: A Literature Review of Catalyst Development. *Catal. Surv. Asia* **2012**, *16*, 183–197.

(57) Sun, Y.-F.; Wang, M.-N.; Luo, J.-L. In-Situ Exsolution of Nano Transition Metal Particles on Lanthanum Chromite Perovskite Anode for Solid Oxide Fuel Cells. *ECS Trans.* **2015**, *68*, 1541–1548.

(58) Papargyriou, D.; Miller, D. N.; Sirt Irvine, J. T. Exsolution of Fe–Ni Alloy Nanoparticles from $(\text{La,Sr})(\text{Cr,Fe,Ni})\text{O}_3$ Perovskites as Potential Oxygen Transport Membrane Catalysts for Methane Reforming. *J. Mater. Chem. A* **2019**, *7*, 15812–15822.

(59) Vert, V. B.; Melo, F. V.; Navarrete, L.; Serra, J. M. Redox stability and electrochemical study of nickel doped chromites as anodes for H_2/CH_4 -fueled solid oxide fuel cells. *Appl. Catal., B* **2012**, *115–116*, 346–356.

(60) Otsuka, K.; Wang, Y.; Sunada, E.; Yamanaka, I. Direct Partial Oxidation of Methane to Synthesis Gas by Cerium Oxide. *J. Catal.* **1998**, *175*, 152–160.

(61) Li, D.; Xu, R.; Gu, Z.; Zhu, X.; Qing, S.; Li, K. Chemical-Looping Conversion of Methane: A Review. *Energy Technol.* **2019**, 1900925.

(62) Davenport, T. C.; Kemei, M.; Ignatowich, M. J.; Haile, S. M. Interplay of Material Thermodynamics and Surface Reaction Rate on the Kinetics of Thermochemical Hydrogen Production. *Int. J. Hydrogen Energy* **2017**, *42*, 16932–16945.

(63) Ignatowich, M. J.; Bork, A. H.; Davenport, T. C.; Rupp, J. L. M.; Yang, C.-k.; Yamazaki, Y.; Haile, S. M. Impact of Enhanced Oxide Reducibility on Rates of Solar-Driven Thermochemical Fuel Production. *MRS Commun.* **2017**, *7*, 873–878.

(64) Ackermann, S.; Sauvin, L.; Castiglioni, R.; Rupp, J. L. M.; Scheffe, J. R.; Steinfeld, A. Kinetics of CO_2 Reduction over Nonstoichiometric Ceria. *J. Phys. Chem. C* **2015**, *119*, 16452–16461.

(65) Zhang, J.; Haribal, V.; Li, F. Perovskite Nanocomposites as Effective CO_2 -Splitting Agents in a Cyclic Redox Scheme. *Sci. Adv.* **2017**, *3*, No. e1701184.

(66) Chen, Y.; Zhu, X.; Li, K.; Wei, Y.; Zheng, Y.; Wang, H. Chemical Looping Co-Splitting of $\text{H}_2\text{O}-\text{CO}_2$ for Efficient Generation of Syngas. *ACS Sustainable Chem. Eng.* **2019**, *7*, 15452–15462.

(67) Qin, Q.; Wu, G.; Chen, S.; Doherty, W.; Xie, K.; Wu, Y. Perovskite Titanate Cathode Decorated by In-Situ Grown Iron Nanocatalyst with Enhanced Electrocatalytic Activity for High-

Temperature Steam Electrolysis. *Electrochim. Acta* **2014**, *127*, 215–227.

(68) Li, S.; Qin, Q.; Xie, K.; Wang, Y.; Wu, Y. High-Performance Fuel Electrodes Based on $\text{NbTi}_{0.5}\text{M}_{0.5}\text{O}_4$ ($\text{M} = \text{Ni}, \text{Cu}$) with Reversible Exsolution of the Nano-Catalyst for Steam Electrolysis. *J. Mater. Chem. A* **2013**, *1*, 8984–8993.

(69) Schneider, C. A.; Rasband, W. S.; Eliceiri, K. W. NIH Image to ImageJ: 25 Years of Image Analysis. *Nat. Methods* **2012**, *9*, 671–675.

(70) Carrillo, A. J.; Bork, A. H.; Moser, T.; Sediva, E.; Hood, Z. D.; Rupp, J. L. M. Modifying $\text{La}_{0.6}\text{Sr}_{0.4}\text{MnO}_3$ Perovskites with Cr Incorporation for Fast Isothermal CO_2 -Splitting Kinetics in Solar-Driven Thermochemical Cycles. *Adv. Energy Mater.* **2019**, *9*, 1803886.